Vietnam Journal of Catalysis and Adsorption
Tạp chí xúc tác và hấp phụ Việt Nam

https://jca.edu.vn

Synthesis of g-C_3N_4@Fe-UiO-66-NH_2 composite photocatalyst for persulfate-assisted degradation of 2,4,6-trinitroresorcinol under visible-light irradiation

Do Tuyet Nhung[1], Dao Minh Hoang[1], Hoang Thi Ngoc Anh[1], Le Hai Dang[1],
Nguyen Thi Van Anh[2,3], Nguyen Thi Thu Hoa[4], Tran Quang Dat[4], Nguyen Trung Dung[4,*]

[1] *Faculty of chemistry, HaNoi National University of Education, 136 Xuan Thuy street, Cau Giay ward, Hanoi, Vietnam.*
[2] *International Analysis Center, University of Industry and Trade, Ho Chi Minh City, Vietnam*
[3] *Faculty of Environment and Natural Resources, Ho Chi Minh City University of Technology (HCMUT), 268 Ly Thuong Kiet Street, District 10, Ho Chi Minh City, Vietnam*
[4] *Faculty of Physics and Chemical Engineering, Le Quy Don Technical University, 236 Hoang Quoc Viet street, Nghia Do ward, Hanoi, Vietnam.*
**Email: ntdung@lqdtu.edu.vn*

ARTICLE INFO

Received: 25/05/2026
Accepted: 29/06/2026
Published: 30/06/2026

Keywords:
Photocatalyst;
g-C_3N_4@Fe-UiO-66-NH_2;
persulfate activation;
visible; 2,4,6-trinitroresorcinol

ABSTRACT

This study reports the synthesis of a g-C_3N_4@Fe-UiO-66-NH_2 (CN@FU) composite photocatalyst for persulfate-assisted degradation of 2,4,6-trinitroresorcinol (TNR) under visible-light irradiation. The composite was successfully fabricated from g-C_3N_4 and Fe-UiO-66-NH_2, and its structural, morphological, textural, optical, and charge-transfer properties were confirmed by XRD, FTIR, SEM–EDX, BET, UV–Vis DRS, and PL analyses. The CN@FU composite exhibited enhanced visible-light absorption, suppressed electron–hole recombination, and a mesoporous structure with a high specific surface area, providing favorable conditions for pollutant adsorption and persulfate activation. Under optimized conditions, the CN@FU/$Na_2S_2O_8$/visible-light system achieved 91.45% TNR removal within 120 min. Quenching experiments revealed that multiple reactive species were involved in the degradation process, with singlet oxygen ($^1O_2$) playing the dominant role, while $O_2^{\bullet-}$, $SO4^{\bullet-}$/$^{\bullet}OH$, and h^+ also contributed. These findings demonstrate that CN@FU is an efficient visible-light-driven photocatalyst for persulfate activation and holds great potential for the treatment of TNR-contaminated wastewater.

Introduction

2,4,6-trinitroresorcinol (TNR) is an aromatic nitro compound widely used in the production of explosives, dyes, and various chemical industries. Wastewater containing TNR is characterized by its intense yellow color, high toxicity, and low biodegradability. The presence of TNR in water, even at low concentrations, can cause adverse effects such as cytotoxicity, impacts on the nervous system, skin irritation, and potential risks of mutagenicity or carcinogenicity. Due to its persistence and resistance to natural degradation, TNR can remain in water for extended periods, entering the biological chain and posing serious risks to human health [1]. Therefore, the removal of TNR from aqueous environments through the development of advanced materials is of great urgency. Various methods, including adsorption, biological treatment, and advanced oxidation processes, have been investigated for the removal of TNR from wastewater. However,

https://doi.org/10.62239/jca.2026.030

conventional techniques often suffer from low degradation efficiency or incomplete mineralization due to the high stability and toxicity of TNR. Among these approaches, photocatalytic degradation has attracted considerable attention because of its high efficiency, environmental friendliness, and ability to utilize solar energy for the generation of reactive species capable of completely degrading refractory organic pollutants. Therefore, photocatalysis is considered a promising strategy for effective TNR removal from aqueous environments.

Advanced oxidation processes based on persulfate (PS) activation under visible light have emerged as promising solutions owing to their ability to generate highly reactive oxygen species (ROS), such as sulfate radicals ($SO_4^{\bullet-}$), hydroxyl radicals ($^{\bullet}OH$), superoxide ($O_2^{\bullet}$) and singlet oxygen ($^1O_2$). Compared with conventional $^{\bullet}OH$-based systems, PS-based AOPs offer distinct advantages, including broader pH adaptability, longer radical lifetimes (30–40 μs), and higher redox potentials (2.5–3.1 V) [2]. However, the practical application of PS requires effective activation strategies to overcome its inherent stability.

Graphitic carbon nitride (g-C_3N_4), a metal-free semiconductor, is capable of activating persulfate (PS) under visible light, while exhibiting high mechanical stability and a relatively narrow band gap of approximately 2.7 eV [3-4]. However, a major limitation of g- C_3N_4 is the rapid recombination of photoinduced electron–hole pairs, which reduces its photocatalytic efficiency. In Vietnam, g-C_3N_4-based photocatalysts have attracted increasing research interest in recent years. Several domestic studies have focused on modifying pristine g-C_3N_4 through elemental doping, surface functionalization, and the construction of semiconductor heterojunctions to improve visible-light absorption, promote photogenerated charge separation, and enhance photocatalytic activity toward persistent organic pollutants [5-6]. These studies have provided an important foundation for the development of advanced g-C_3N_4-based photocatalytic systems for environmental remediation. Nevertheless, the application of modified g-C_3N_4 materials for visible-light-driven persulfate activation and the degradation of highly stable nitroaromatic pollutants remains insufficiently investigated in Vietnam.

Metal–organic frameworks (MOFs) exhibit many excellent properties, such as intrinsic porous structures, large specific surface areas, and tunable architectures, enabling them to expose numerous accessible active sites with high catalytic activity [4]. Among various MOF families, UiO-66-NH_2 has attracted considerable attention owing to its potential in diverse photocatalytic applications, including water splitting [7], H_2O_2 production [8], CO_2 reduction [9], and the degradation of recalcitrant organic pollutants [10], due to its exceptional chemical and thermal stability in aqueous environments.

Previous studies have demonstrated that integrating g-C_3N_4 with UiO-66-NH_2 is an effective strategy to tailor visible-light absorption and optimize the band structure of MOF/carbon nitride-based photocatalysts. The interfacial heterojunction formed between these two components can accelerate photogenerated charge transfer, promote electron–hole separation, and suppress charge recombination, thereby significantly improving photocatalytic performance toward the degradation of aqueous pollutants [11-12]

In this study, g-C_3N_4@ Fe-UiO-66-NH_2 was synthesized from individual components and applied as a photocatalyst for persulfate (PS) activation to degrade TNR in aqueous solution. The nanocomposites were characterized using XRD, FT-IR, SEM, EDX, BET, UV–Vis DRS, and PL analyses. The effects of various parameters, including the catalytic system, catalyst ratio, catalyst dosage, PS concentration, and pH, were investigated. In addition, the reactive species generated in the CN@FU/PS/visible-light system were identified through quenching experiments.

Experimental

Chemicals and reagents

The chemicals used were of high purity and did not require further purification, including zirconium tetrachloride ($ZrCl_4$), iron(III) chloride hexahydrate ($FeCl_3.6H_2O$), 2-aminoterephthalic acid (NH_2-BDC), N,N-dimethylformamide (DMF), urea (CH_4N_2O), ethanol (EtOH), sodium persulfate ($Na_2S_2O_8$-PS), tert butyl alcohol (TBA), ascorbic acid (AA), ammonium oxalate (AO), L-histidine, and 2,4,6-trinitroresorcinol supplied by Sigma Aldrich (USA). Sulfuric acid (H_2SO_4) and sodium hydroxide (NaOH) were provided by Xilong (China).

Preparation of g-C_3N_4, Fe-UiO-66-NH_2 and g-C_3N_4@ Fe-UiO-66-NH_2

The materials g-C_3N_4 (CN), Fe-UiO-66-NH_2 (FU) and g-C_3N_4@ Fe-UiO-66-NH_2 (CN@FU) were synthesized as shown in Fig. 1.

CN was synthesized by the direct thermal polymerization of urea. Specifically, 10 g of urea was placed in a porcelain crucible and covered with

aluminum foil. The sample was first heated from 30 °C to 300 °C at a heating rate of 5 °C min^{-1} and maintained at 300 °C for 30 min. The temperature was then increased to 525 °C at a heating rate of 2 °C min^{-1} and kept at this temperature for 2.5 h. After calcination, the obtained material was ground to obtain a yellow fine powder of CN[13].

FU was synthesized via a hydrothermal method. 2mM $ZrCl_4$ (0.466 g), 2mM $FeCl_3.6H_2O$ (0.540 g), and 4mM NH_2-BDC (0.725 g) were dissolved in 60 mL of DMF under stirring. The resulting solution was transferred into a 100 mL Teflon-lined stainless steel autoclave, sealed, and heated at 120 °C for 24 h. After cooling naturally to room temperature, the solid product was collected by centrifugation at 5000 rpm for 5 min or by vacuum filtration. The product was washed several times with DMF, ethanol, and distilled water (three times each) and finally dried at 80 °C for 8 h[14].

For the synthesis of CN@FU, 1.0 g of g-C_3N_4 was dispersed in 30 mL of ethanol and ultrasonicated for 45 min. Subsequently, 1.0 g of Fe-UiO-66-NH_2 was added to the dispersion. The mixture was ultrasonicated for an additional 5 min and then stirred for 24 h. The obtained white solid product was collected after natural solvent evaporation and dried at 80 °C for 12 h.

Characterization

The surface morphology of the CN@FU composite was examined by scanning electron microscopy (SEM) (FE-SEM, JEOL JSM-6701F, Japan) at an accelerating voltage of 3.0 kV. The crystalline phase composition of the samples was analyzed by X-ray diffraction (XRD) (XRD, D8 Advance, Bruker, Germany) using Cu Kα radiation (λ = 1.5406Å) over a 2θ range of 5–80°. The elemental composition of the solid material was determined by energy-dispersive X-ray spectroscopy (EDX) (EMSA/MAS, Japan). The specific surface area and porous structure of the materials were determined using the Brunauer-Emmett-Teller (BET) methods (Micromeritics TriStar II Plus 2.03). The band gap energy and light absorption properties of the material were evaluated using UV–Vis diffuse reflectance spectroscopy (UV–Vis DRS) (V670, Jasco, Japan). The photoluminescence properties and the recombination of electron–hole pairs were investigated by photoluminescence spectroscopy (PL) in the wavelength range of 350–600nm.

Photocatalytic degradation of TNR over CN@FU

The photocatalytic experiments were carried out under visible light irradiation to evaluate the degradation efficiency of TNR using the CN@FU/PS system. A predetermined amount of photocatalyst was dispersed in 100 mL of 20 mg/L TNR, and the suspension was magnetically stirred in the dark for 30 min to achieve adsorption–desorption equilibrium prior to illumination. Subsequently, PS was added to the suspension while oxygen was continuously supplied throughout the reaction process. The photocatalytic reaction was carried out under a 40 W LED light source (Emission wavelength 446 nm) positioned 9 cm above the solution surface, and the reaction temperature was maintained at 25 °C.

During the reaction (120 minutes), aliquots were withdrawn at predetermined time intervals and centrifuged at 4000 rpm for 5 min to remove the catalyst. The residual concentration of TNR was determined by UV–Vis spectrophotometry at a wavelength of 400 nm. The effects of various factors, including catalyst dosage, $Na_2S_2O_8$ concentration, initial TNR concentration, and solution pH, on the degradation efficiency were systematically investigated. The pollutant removal efficiency was determined using the following formula:

$$H\ (\%) = (1 - \frac{C_t}{C_o}).100 = (1 - \frac{A_t}{A_o}).100$$

Here, C_o and A_o represent the initial concentration and absorbance of TNR, while C_t and A_t denote the concentration and absorbance at time t.

Results and discussion

Characterization of materials

The crystal structures of the CN, FU and CN@FU were determined by X-ray diffraction (XRD) spectroscopy (Fig.1a). The XRD pattern of pristine CN exhibits two characteristic diffraction peaks at 2θ values of 13.1° and 27.5°, corresponding to the (100) and (002) crystal planes, respectively. The peak at 13.1° is attributed to the in-plane structural packing of tri-s-triazine units, while the strong diffraction peak at 27.5° is associated with the interlayer stacking of conjugated aromatic systems, confirming the successful formation of graphitic carbon nitride with good crystallinity ((JCPDS số 87–1526) [3].

For the FU material, characteristic diffraction peaks are observed at 2θ values of approximately 7.5°, 8.5°, 12.0°, 14.8°, 17.1°, and 25.8°, corresponding to the (111), (002), (222), (400), and (600) crystal planes of the UiO-66 framework, respectively, which is consistent with previous reports [7-8]. The low crystallinity of Fe-UiO-66-NH2 may be due to competitive coordination between Fe^{3+} and Zr^{4+} centers in the formation of the material [16].

https://doi.org/10.62239/jca.2026.030

The XRD pattern of the synthesized CN@FU composite contains the characteristic diffraction peaks of both g-C_3N_4 and Fe-UiO-66-NH_2, confirming the successful formation of the composite structure without destroying the crystallinity of the parent materials.

The FTIR spectra of CN, FU, and the synthesized composite are shown in Fig.1b. For pristine g-C_3N_4, the characteristic absorption bands observed in the range of 1200–1650 cm^{-1} are attributed to the stretching vibrations of C–N and C=N heterocycles, while the broad band around 3070-3284 cm^{-1} corresponds to N–H stretching vibrations [12]. In the spectrum of Fe-UiO-66-NH_2, the absorption peaks in the region of 1400–1600 cm^{-1} are associated with the symmetric and asymmetric stretching vibrations of carboxylate groups from the organic linker. The peaks at 650 cm^{-1} and 767 cm^{-1} are characteristic of the Fe–O and Zr–O bonds, respectively, in FU [14]. The FTIR spectrum of the CN@FU composite contains the characteristic bands of both CN and FU, confirming the successful formation of the composite structure. In addition, slight shifts and intensity changes in several absorption peaks suggest strong interfacial interactions between CN and FU.

UV–Vis DRS (Fig 1c) results show that CN mainly absorbs light in the visible region, with an absorption edge at approximately 450 nm, which is characteristic of CN with a band gap of about 2.7 eV. In contrast, FU exhibits broader light absorption owing to the presence of $–NH_2$ ligands and Fe centers in the FU framework, which may enhance ligand-to-metal charge transfer. For the CN@FU composite, the visible-light absorption intensity is significantly enhanced, and the absorption edge shows a red shift compared with pristine CN. This indicates that the formation of the heterostructure improves light-harvesting ability and promotes the separation of photogenerated electron–hole pairs [11].

As shown in Fig. 1d, the band gap energies of CN, FU, and CN@FU, calculated using the Tauc method, are 2.70, 2.12, and 2.60 eV, respectively. The lower band gap of CN@FU compared with CN suggests that the composite possesses an expanded visible-light absorption range, which is more favorable for photoinduced electron–hole generation. This enhanced photoexcitation ability may contribute to more efficient persulfate activation and improved TNR degradation under visible-light irradiation.

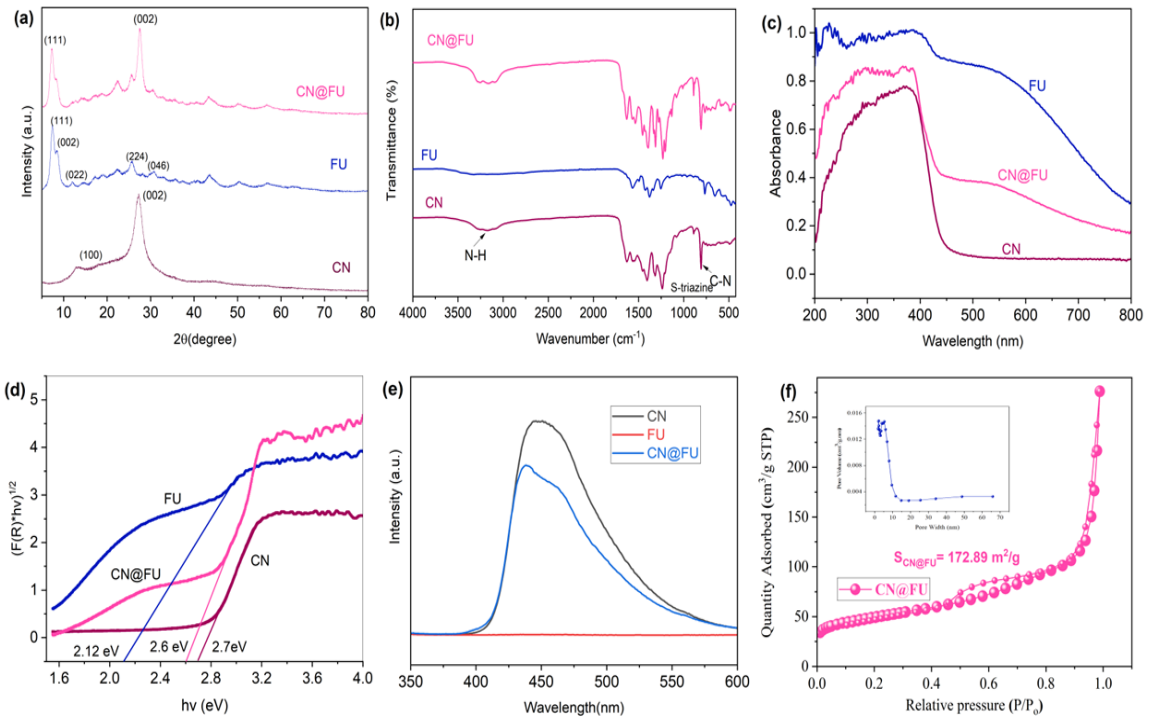

Fig. 1. Structural, optical, and textural characterization of CN, FU, and CN@FU: (a) XRD patterns, (b) FTIR spectra, (c) UV–Vis DRS spectra, (d) Tauc plots, (e) PL spectra, and (f) N_2 adsorption–desorption isotherm and pore-size distribution of CN@FU

The PL spectra (Fig.1e) show that all samples exhibit emission peaks at approximately 440–470 nm, which are characteristic of photogenerated electron–hole recombination in g-C_3N_4. Among the samples, CN displays the highest PL intensity, indicating rapid charge recombination and, consequently, limited utilization of electrons and holes in the photocatalytic reaction.

In contrast, FU shows very weak PL intensity, suggesting lower luminescence activity and a different electron-transfer behavior associated with the Fe-containing MOF structure. Notably, the CN@FU composite exhibits a markedly lower PL intensity than CN, demonstrating that the heterostructure formed between CN and FU effectively promotes charge separation and transfer, thereby suppressing e^-/h^+ recombination. This reduced PL intensity provides evidence for the enhanced photocatalytic potential of CN@FU, which is consistent with its improved TNR degradation performance under visible-light irradiation [17].

The BET analysis of CN@FU (Fig.1f) shows that the N_2 adsorption–desorption isotherm belongs to a typical type IV isotherm with a distinct hysteresis loop at high relative pressure (P/P_0 > 0.8), indicating the presence of a mesoporous structure. This result suggests that the material possesses a well-developed pore system, which is favorable for pollutant diffusion and enhances the contact between the catalyst and the reaction solution.

The BET results of the synthesized CN@FU show a specific surface area of 172.89 m^2/g. The pore size distribution reveals that the dominant pores are mainly distributed in the range of 2–8 nm, together with the presence of several larger pores attributed to interparticle voids. Therefore, the synthesized material possesses a relatively large surface area together with a hierarchical porous structure, providing abundant active sites and thereby enhancing photocatalytic performance.

The SEM images of CN@FU (Fig.2a-b) show a heterogeneous surface structure, consisting of aggregated particle clusters interspersed with wrinkled sheet-like layers/fragments characteristic of g-C_3N_4. At higher magnification, the Fe-UiO-66-NH_2 nanoparticles are distributed on the surface or between the g-C_3N_4 layers, forming a rough structure with numerous pores and voids. The intimate contact between the Fe-UiO-66-NH_2 phase and g-C_3N_4 indicates the successful formation of the composite rather than a simple physical mixture. The porous and rough morphology, together with the dispersion of active particles, may increase the number of reactive sites, enhance pollutant adsorption, and facilitate charge transfer in the photocatalytic/persulfate activation system.

The EDX spectrum of CN@FU (Fig. 2c) reveals the presence of C, N, O, Zr, and Fe, with corresponding contents of 20.1, 6.6, 72.6, 0.5 and 0.2 wt.%. The C and N signals are mainly attributed to the g-C_3N_4 phase and the amino-functionalized organic linker, whereas Zr and O are characteristic constituents of the UiO-66-NH_2 framework. The presence of Fe confirms that Fe species were incorporated into the Fe-UiO-66-NH_2 component. Moreover, no additional major elemental signals were detected, indicating the absence of detectable elemental impurities. The EDX mapping images (Fig. 2d) show a relatively uniform distribution of C, N, O, Zr, and Fe throughout the analyzed region. Combined with the XRD and FTIR results, the EDX analysis supports the successful formation of the CN@FU composite.

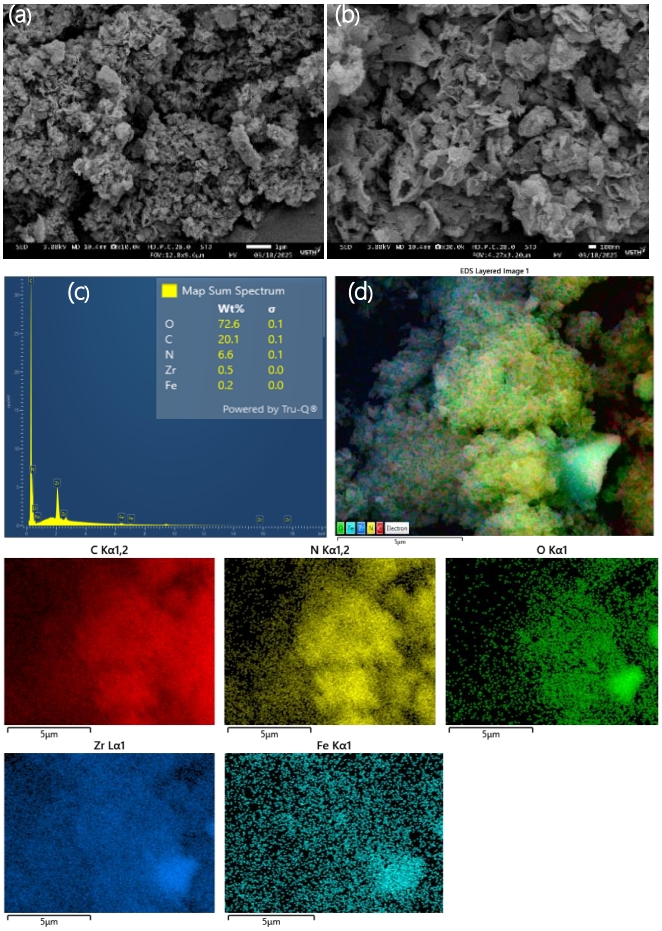

Fig. 2. SEM images (a, b); (c) EDX spectrum and (d) EDX mapping images of CN@FU.

Organic contaminants degradation efficiency by CN @FU

The TNR degradation efficiency was affected by several operational factors, including the catalytic system, catalyst dosage, $Na_2S_2O_8$ concentration, and solution pH, as shown in Fig. 3. Fig. 3a presents the effect of different catalytic systems on TNR degradation under visible-light irradiation. After 120 min, the degradation efficiency increased in the following order: PS/Vis (2.85%) < CN@FU/Dark (3.27%) < CN@FU/Vis (5.67%) < FU/PS/Vis (36.25%) < CN/PS/Vis (57.74%) < CN@FU/PS/Vis (91.45%). The CN@FU/PS/Vis system exhibited the highest degradation efficiency, which was approximately 32.1 and 16.13 times higher than those of

https://doi.org/10.62239/jca.2026.030

PS/Vis and CN@FU/Vis, respectively. This result indicates that the combined effect of the CN@FU catalyst, persulfate oxidant, and visible light significantly promoted the generation of reactive oxygen species in the CN@FU/PS/Vis system [15]. Compared with FU/PS/Vis and CN/PS/Vis, the CN@FU/PS/Vis system showed a markedly enhanced TNR degradation efficiency. This improvement can be attributed to the formation of heterojunctions in the CN@FU composite, which facilitated charge separation and suppressed the recombination of photogenerated electron–hole pairs. The photogenerated electrons and holes could react with dissolved O_2 and H_2O to produce $O_2^{\bullet-}$ and $^{\bullet}OH$, respectively. Meanwhile, persulfate was activated on the catalyst surface to generate $SO_4^{\bullet-}$ and additional $^{\bullet}OH$ radicals. These reactive species collectively contributed to the efficient degradation of TNR [16]. Therefore, the CN@FU/PS/Vis system was selected for subsequent experiments.

Fig. 3b shows the effect of CN@FU catalyst dosage on TNR degradation efficiency. As the catalyst concentration increased from 0 to 200 mg/L, the TNR removal efficiency increased from 2.85% to 75.93%. This improvement can be attributed to the porous structures of both CN and FU, which provide a larger contact surface area and facilitate the adsorption of TNR molecules onto the catalyst surface. In addition, the increased catalyst dosage supplied more active catalytic sites, thereby promoting the activation of persulfate under visible-light irradiation and enhancing the generation of reactive oxygen species. As a result, TNR degradation efficiency increased with increasing CN@FU dosage.

However, when the catalyst dosage was further increased to 300 and 400 mg/L, the degradation efficiency slightly decreased. This decline may be related to the reduced light penetration caused by the darker and more turbid catalyst suspension at high catalyst concentrations. Excess catalyst particles can also shield active sites from light irradiation and reduce the effective illuminated surface area, thereby limiting photocatalytic activation [18]. Therefore, 200 mg/L was selected as the optimal CN@FU catalyst dosage for subsequent experiments.

As shown in Fig. 3c, the effect of persulfate concentration on TNR degradation was also investigated. At PS concentrations of 0, 0.42, 0.84, 1.26, 1.68, and 2.10 mM, the TNR degradation efficiencies were 5.57%, 37.21%, 80.00%, 91.45%, 97.66%, and 98.17%, respectively. At low PS concentrations, the degradation efficiency was relatively limited because the amount of persulfate available for activation was insufficient, resulting in lower production of $SO_4^{\bullet-}$ radicals. Increasing the PS concentration enhanced TNR degradation by generating more reactive radical species. However, when the PS concentration was increased beyond 1.26 mM, the improvement in degradation efficiency became less pronounced [19]. Although 1.68 and 2.10 mM PS gave slightly higher removal efficiencies, the increase was relatively small compared with the additional oxidant dosage. Therefore, 1.26 mM was selected as the appropriate PS concentration for further experiments.

pH is a key factor influencing the catalyst surface properties, pollutant speciation, and generation of reactive radicals, thereby determining TNR removal efficiency. As shown in Fig.3d, TNR degradation strongly depends on pH, increasing from 68.76% at pH 3 to a maximum of 91.45% at pH 4, followed by a decrease to 75.23%, 71.95%, and 71.31% at pH 5, 7, and 9, respectively. This result indicates that a mildly acidic condition is most favorable for the CN@FU/PS/visible-light system, likely due to enhanced persulfate activation and promoted generation of $SO_4^{\bullet-}$ and •OH. In contrast, under strongly acidic or neutral-to-alkaline conditions, the lower degradation efficiency may be attributed to radical scavenging, changes in dominant ROS species, and unfavorable electrostatic interactions between TNR and the catalyst surface. This trend agrees with recent studies reporting that pH plays a decisive role in persulfate activation, $SO_4^{\bullet-}$ to •OH transformation, and the degradation efficiency of organic pollutants [20].

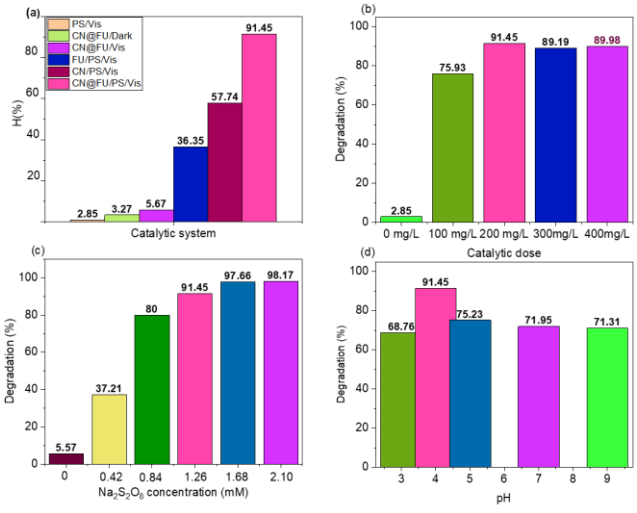

Fig.3: Effect of the catalytic system (a), catalyst dosage (b), $Na_2S_2O_8$ concentration (c) and initial pH (d)
The experiments were conducted under the following conditions: [TNR] = 20 mg/L; catalyst dosage =0-400 mg/L, PS concentration=0-2.1mM, pH=3-9, T=25 °C; and irradiation time = 120 min.

Proposed mechanism for TNR degradation in the CN@FU/PS/visible light system

In the CN@FU/PS/visible light system, several reactive species, including •OH, SO_4•$^-$, O_2•$^-$, $^1O_2$, and photogenerated holes (h^+), may be generated during TNR degradation. To identify the dominant reactive species, quenching experiments were performed. Ethanol (EtOH) was used to scavenge both •OH and SO_4•$^-$, while tert-butanol (TBA) was employed as a selective •OH scavenger. In addition, ammonium oxalate (AO), ascorbic acid (AA), and L-histidine were used to quench h^+, O_2•$^-$, and $^1O_2$, respectively.

In the absence of scavengers, the CN@FU/PS/visible-light system achieved a TNR degradation efficiency of 91.45% (Fig.4). The addition of L-histidine caused the degradation efficiency to decrease sharply to only 1.05%, indicating that singlet oxygen ($^1O_2$) plays a dominant role in TNR degradation. The degradation efficiency decreased to 20.68% in the presence of ethanol, which scavenges both SO_4•$^-$ and •OH, whereas it remained at 58.14% after the addition of tert-butanol, a preferential •OH scavenger. The stronger inhibition by ethanol than by tert-butanol indicates that SO_4•$^-$ contributed more significantly than •OH to TNR degradation. Furthermore, the degradation efficiencies decreased to 18.25% and 31.12% in the presence of ascorbic acid and ammonium oxalate, respectively, indicating the involvement of O_2•$^-$ and photogenerated holes. These results demonstrate that TNR degradation proceeds through a multi-reactive-species mechanism dominated by $^1O_2$, with additional contributions from SO_4•$^-$, O_2•$^-$, •OH, and h+.

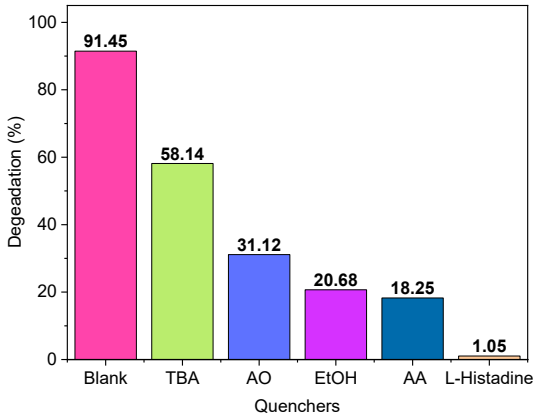

Fig. 4: Reactive species trapping experiment of CN@FU/PS/Visible ([Catalyst] = 200 mg/L, [PS] = 1.26 mM, T = 25 °C, pH = 4.0, TBA=EtOH=100mM, [AO]=[AA]=[Histidine]=1mM)

Owing to the intimate interfacial contact between the two semiconductors, the CN@FU heterostructure operates through a direct Z-scheme charge-transfer pathway, in which the photogenerated electrons in the conduction band (CB) of Fe-UiO-66-NH_2 preferentially recombine with the holes in the valence band (VB) of g-C_3N_4. This interfacial recombination effectively suppresses the bulk electron–hole recombination, as evidenced by the reduced photoluminescence (PL) intensity of CN@FU, while simultaneously preserving the highly reductive electrons in the CB of g-C_3N_4 and the strongly oxidative holes in the VB of Fe-UiO-66-NH_2. Consequently, the heterostructure maintains high redox capability together with efficient charge separation.

Within this Z-scheme heterojunction, g-C_3N_4 primarily functions as the visible-light absorber and reduction component. The retained electrons in the CB of g-C_3N_4 reduce dissolved O_2 to generate O_2•$^-$ and directly activate peroxydisulfate ($S_2O_8^{2-}$) through one-electron cleavage of the O–O bond, producing SO_4•$^-$.

$$O_2 + e^- \rightarrow O_2\text{•}^-$$
$$S_2O_8^{2-} + e^- \rightarrow SO_4\text{•}^- + SO_4^{2-}$$

Meanwhile, Fe-UiO-66-NH_2 serves as a porous adsorptive and catalytic framework that enriches TNR and $S_2O_8^{2-}$ near the active interface, thereby facilitating interfacial redox reactions. More importantly, the Fe centers act as electron-transfer mediators and catalytic sites for persulfate activation. Surface Fe(III) species are photoreduced by the retained electrons to Fe(II), which subsequently react with $S_2O_8^{2-}$ to regenerate Fe(III) while producing additional SO_4•$^-$ radicals. Therefore, the Fe(III)/Fe(II) redox cycle provides an additional and continuous pathway for persulfate activation, further enhancing reactive oxygen species generation.

$$\equiv Fe^{II} + S_2O_8^{2-} \rightarrow \equiv Fe^{III} + SO_4\text{•}^- + SO_4^{2}$$
$$\equiv Fe^{III} + e^- \rightarrow \equiv Fe^{II}$$

The generated SO_4•$^-$ radicals can directly oxidize TNR or react with H_2O/OH^- to form •OH. Meanwhile, O_2•$^-$ can participate directly in pollutant oxidation and may also contribute to the generation of $^1O_2$ through secondary reactions involving O_2•$^-$ and other reactive intermediates. Photogenerated holes (h^+) can directly oxidize TNR and its degradation intermediates.

$$SO_4\text{•}^- + H_2O \rightarrow SO_4^{2-} + \text{•}OH + H^+$$
$$SO_4\text{•}^- + OH^- \rightarrow SO_4^{2-} + \text{•}OH$$
$$2O_2\text{•}^- + 2H^+ \rightarrow {}^1O_2 + H_2O_2$$
$$2O_2\text{•}^- + SO_4\text{•}^- \rightarrow {}^1O_2 + SO_4^{2-}$$

Based on the radical-scavenging experiments, $^1O_2$ is identified as the dominant reactive oxygen species, while O_2•$^-$, SO_4•$^-$, •OH, and h^+ also participate in TNR degradation. Overall, the superior photocatalytic performance of the CN@FU/PDS/visible-light system originates from the synergistic combination of the direct

https://doi.org/10.62239/jca.2026.030

Z-scheme charge-transfer mechanism, efficient visible-light harvesting by g-C_3N_4, preservation of strongly reductive electrons and strongly oxidative holes, continuous Fe(III)/Fe(II)-mediated persulfate activation, and the porous adsorption capability of Fe-UiO-66-NH_2, collectively promoting the generation of multiple reactive oxygen species and the rapid degradation of TNR.

As summarized in Table 1, g-C_3N_4-based photocatalysts coupled with persulfate generally achieved high removal efficiencies (82.8–99.7%) for various organic pollutants under visible-light irradiation. The CN@FU/PS/visible-light system exhibited a competitive TNR degradation efficiency of 91.45%, confirming the beneficial role of the CN–Fe-UiO-66-NH_2 heterojunction in promoting charge separation and persulfate activation.

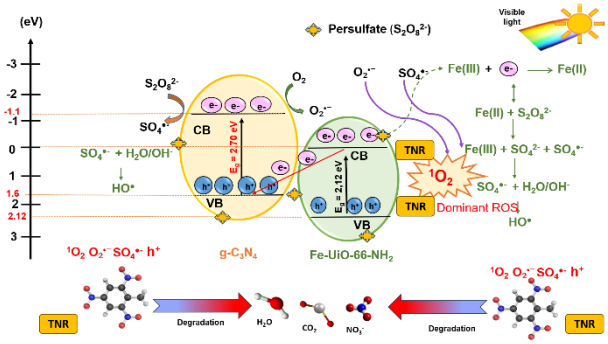

Fig. 5: Proposed mechanism of persulfate activation and TNR degradation in the CN@FU/PS/visible-light system.

Table 1. Comparison of organic pollutant degradation by g-C_3N_4-based photocatalysts coupled with persulfate under visible-light irradiation

Catalyst	Optimal conditions	Efficiency of pollutant degradation (%)	References
CN@FU	Catalyst 200 mg/L, PS : 1.26 mM, TNR : 20 mg/L, pH=4, Visible light 40 W (LED lamp) Duration: 120 minutes.	91.45% ROS : ·OH, $SO_4^{\bullet-}$, $\cdot O_2^-$ $^1O_2$	This study
CFO/ CNs	Catalyst: 50 mg; PMS: 1.0 mM; LFX: 50 mg/L; pH = 7; Visible light 300 W (Xenon lamp) ; Duration: 60 minutes.	99.1% ROS: ·OH, $SO_4^{\bullet-}$, $\cdot O_2^-$, $^1O_2$	[21]
CN@$CoFe_2O_4$/ Fe_2O_3	Catalyst: 333 mg/L; PS:2.8mM; TC: 30 mg/L; pH = 7; Visible light 300 W (Xenon lamp); Duration: 80 minutes.	99.7% ROS: ·OH, $SO_4^{\bullet-}$	[22]
Co_3O_4@P-CN/ α- Fe_2O_3	Catalyst: 500 mg/L; PS: 2mM; BPA: 50 mg/L; pH = 6.8; Visible light 300W (Xenon lamp); Duration: 90 minutes.	99.3% ROS: ·OH, $SO_4^{\bullet-}$, $\cdot O_2^-$	[23]
CN@ MIL-100(Fe)	Catalyst: 2000 mg/L; PS:2 mM; DOX: 10 mg/L; pH = 6.5; Visible light 200W (Xenon lamp) Duration: 30 minutes.	82.8% ROS: ·OH, $SO_4^{\bullet-}$	[24]
$CNBMn_2$	Catalyst: 750 mg/L; PS: 1.5 mM; TC: 10 mg/L; pH = 7; Visible light 300W (Xenon lamp), Duration: 40 minutes.	99.0% ROS: OH, $SO_4^{\bullet-}$, $\cdot O_2^-$, $^1O_2$	[25]
Co, Fe doped GCN	Catalyst: 800 mg/L; PMS: 1.0 mM; TC: 20 mg/L; pH = 6.8; Visible light 300W (Xenon lamp) Duration: 50 minutes.	96% ROS: ·OH, $SO_4^{\bullet-}$, $\cdot O_2^-$, $^1O_2$	[26]

https://doi.org/10.62239/jca.2026.030

Acknowledgement

This research is funded by Vietnam National Foundation for Science and Technology Development (NAFOSTED) under grant number 104.05-2023.18.

Conclusion

In this work, g-C_3N_4, Fe-UiO-66-NH_2, and g-C_3N_4@Fe-UiO-66-NH_2 were successfully synthesized and applied for TNR degradation in a persulfate-assisted visible-light photocatalytic system. The characterization results confirmed the successful formation of the CN@FU heterostructure, which enhanced visible-light absorption, promoted charge separation, and provided abundant active sites for persulfate activation. The CN@FU/PS/visible-light system exhibited superior degradation performance compared with the individual components, achieving 91.45% TNR removal within 120 min under optimized conditions: 20 mg/L TNR, 200 mg/L catalyst, 1.26 mM $Na_2S_2O_8$, pH 4.0, and 25 °C. Radical trapping experiments revealed that $^1O_2$ was the dominant reactive species, with additional contributions from $O_2^{\bullet-}$, $SO_4^{\bullet-}$/$^{\bullet}$OH, and photogenerated holes. Overall, the CN@FU/PS/visible-light system offers an efficient and environmentally friendly strategy for degrading refractory nitroaromatic pollutants in contaminated water.

References

1. H.V. Nguyen, K.N. Do, T.C. Nguyen, Pol. J. Environ. Stud., 30 (2021) 135831. https://doi.org/10.15244/pjoes/135831
2. J. Mao, H. Li, H. Pan, C. Wang, Z. Gu, Y. Bai, J. Qu, Chem. Eng. J., 518 (2025) 164605. https://doi.org/10.1016/j.cej.2025.164605
3. W. Zhang, Y. Hao, C. Fang, X. Dou, J. Liu, J. Water Process Eng., 66 (2024) 106088. https://doi.org/10.1016/j.jwpe.2024.106088
4. M.S. Khan, Y. Li, D.-S. Li, J. Qiu, X. Xu, H.Y. Yang, Nanoscale Adv., 23 (2023) 6318-6348. https://doi.org/10.1039/D3NA00627A
5. V.K. Nguyen, V.N. Nguyen Thi, H.H. Tran, T.P. Tran Thi, T.T. Truong, V. Vo, Bull. Mater. Sci., 44 (2021) 28. https://doi.org/10.1007/s12034-020-02277-2
6. L.N. Thi, N.N. Tri, L.N. Tan, N.M. Vuong, T.L.T. Le, D.T.T. Nu, V. Vo, J. Alloys Compd., 1018 (2025) 179245. https://doi.org/10.1016/j.jallcom.2025.179245
7. B. Abbas, A.V. Ravindra, Mol. Catal., 578 (2025) 115025. https://doi.org/10.1016/j.mcat.2025.115025
8. M.A. Qaiser, J. Li, W. Ren, S. Khan, S.B. Ahmed, W.A. Qureshi, M.H. Abdurahman, W. Wang, Q. Liu, Chem. Eng. J., 525 (2025) 170188. https://doi.org/10.1016/j.cej.2025.170188
9. D. Xu, Z. Zhang, B. Yuan, H. Yan, Y. Hou, Y. Hou, X. Ren, Y. Liao, Appl. Surf. Sci., 686 (2025) 162225. https://doi.org/10.1016/j.apsusc.2024.162225
10. K. Lin, B. Cao, X. Deng, Q. Li, Y. Wang, Appl. Organomet. Chem., 5 (2025) e7970. https://doi.org/10.1002/aoc.7970
11. Z. Huang, H. Yu, L. Wang, X. Liu, S. Ren, J. Liu, J. Hazard. Mater., 436 (2022) 129052. https://doi.org/10.1016/j.jhazmat.2022.129052
12. S. Duan, J. Liu, X. Meng, W. Zhang, Q. Liu, G. Zhao, J. Zhao, J. Li, Sep. Purif. Technol., 377 (2025) 134318. https://doi.org/10.1016/j.seppur.2025.134318
13. Y. Huang, G. Lin, Z. Hua, X. Chen, X. Xu, Diam. Relat. Mater., 304 (2024) 110614. https://doi.org/10.1016/j.diamond.2023.110614
14. M. Qian, Y. Hou, D. Zhang, Z. Long, X. Jiang, H. Zhao, F. Sun, A. Alireza, C. Sun, Colloids Surf. A Physicochem. Eng. Asp., 727 (2025) 138354. https://doi.org/10.1016/j.colsurfa.2025.138354
15. N.T. Dung, T.T. Hue, V.D. Thao, N.N. Huy, RSC Adv., 11 (2021) 28496-28507. https://doi.org/10.1039/D1RA03496K
16. Y. Bai, W. Dong, Q. Zhang, H. She, X. Chen, Q. Wang, J. Alloys Compd., 1033 (2025) 181237. https://doi.org/10.1016/j.jallcom.2025.181237
17. R.R. Solís, M.A. Quintana, M.Á. Martín-Lara, A. Pérez, M. Calero, M.J. Muñoz-Batista, Int. J. Mol. Sci., 23 (2022) 12871. https://doi.org/10.3390/ijms232112871
18. L. Luo, C. Cha, D. Meng, W. Zou, L. Xia, F. Jiang, X. Ma, J. Dai, J. Environ. Chem. Eng., 12 (2024) 113489. https://doi.org/10.1016/j.jece.2024.113489
19. H. Zhang, X. Wang, X. Pang, G. Ma, J. Water Process Eng., 72 (2025) 107495. https://doi.org/10.1016/j.jwpe.2025.107495
20. M. Hasanzadeh, Z. Ghaedrahmat, N. Kayedi, N.J. Fard, A. Azari, M. Afsharizadeh, Heliyon, 9 (2023) e21421. https://doi.org/10.1016/j.heliyon.2023.e21421
21. L. Chen, F. Wang, J. Zhang, H. Wei, L. Dang, Environ. Res., 241 (2024) 117653. https://doi.org/10.1016/j.envres.2023.117653
22. S.-W. Lv, J.-M. Liu, N. Zhao, C.-Y. Li, F.-E. Yang, Z.-H. Wang, S. Wang, Sep. Purif. Technol., 253 (2020) 117413. https://doi.org/10.1016/j.seppur.2020.117413
23. V.M. Rangaraj, S. Devaraju, T.G. Reddy, H. Zafar, D.H. Anjum, V. Mittal, Mater. Res. Bull., 179 (2024) 112925. https://doi.org/10.1016/j.materresbull.2024.112925
24. W. Liu, Q. Kang, L. Wang, L. Wen, Z. Li, Colloids Surf. A Physicochem. Eng. Asp., 635 (2022) 128057. https://doi.org/10.1016/j.colsurfa.2021.128057
25. T.G. Nguyen, M.D. Nguyen, T.L. Do, V.T. Dang, V.H. Hoang, T.H. Nguyen, Mater. Res. Express, 12 (2025) 055004. https://doi.org/10.1088/2053-1591/add98e
26. W. Wang, Y. Tai, Q. Wu, S. Shao, Y. Zhao, L. Cai, Q. Liu, Appl. Water Sci., 15 (2025) 133. https://doi.org/10.1007/s13201-025-02476-4